J Solid State Electrochem (2011) 15:711–723
DOI 10.1007/s10008-010-1137-2

ORIGINAL PAPER

Layered molybdenum oxide thin films electrodeposited from sodium citrate electrolyte solution

Dovile Sinkeviciute · Jonas Baltrusaitis · Nijole Dukstiene

Received: 16 April 2010 / Revised: 28 June 2010 / Accepted: 1 July 2010 / Published online: 21 July 2010

Abstract Molybdenum oxide thin films were prepared electrochemically onto the selenium predeposited tin oxide-coated glass substrates using 0.22 M sodium citrate ($C_6H_5Na_3O_7$) solution (pH 8.3) and sodium molybdate as a precursor. Cyclic voltammetry was used to determine the deposition potential effects on molybdenum compound speciation, while quantitative thin film composition was obtained from X-ray photoelectron spectroscopy depth profiles. Thin molybdenum film growth and composition was potential dependant. Predominant molybdenum species was Mo(IV) at all deposition potentials and deposition times. Optical properties of the molybdenum oxide thin films were determined using UV–VIS spectroscopy. The absorption edge varied between 560 and 650 nm, whereas optical band gap values—between 1.79 and 2.19 eV—well within the limits for solar light-induced chemical reactions.

Keywords Molybdenum oxides · Selenium · Electrodeposition · Thin films · Structural and optical properties · XPS

Electronic supplementary material The online version of this article (doi:10.1007/s10008-010-1137-2) contains supplementary material, which is available to authorized users.

D. Sinkeviciute · N. Dukstiene (✉)
Department of Physical Chemistry, Kaunas,
Kaunas University of Technology,
Radvilenu pl. 19,
3028 Kaunas, Lithuania
e-mail: nijole.dukstiene@ktu.lt

J. Baltrusaitis (✉)
Department of Chemistry and Central Microscopy Research Facility, 76 EMRB, University of Iowa,
Iowa City, IA 52242, USA
e-mail: jonas-baltrusaitis@uiowa.edu

Introduction

Nanoscale materials, such as nanowires, nanorods, nanowhiskers, and nanofibers, have stimulated great interest due to their importance in basic scientific research and potential technology applications [1–3]. Electrodeposition is a useful method in obtaining thin films at the nanometer scale that possess many useful properties, such as photocorrosion resistance [4], optical [5, 6], and catalytic activity [7–9]. In this regard, electrolytic molybdenum chalcogenide and oxide-based thin films are particularly attractive due to their rich chemistry produced by the multiple valance states of the metal.

Electrolytically deposited molybdenum oxide is a promising cathode material for lithium batteries due to its stable reversible capacity within 200–250 $mAhg^{-1}$ [10]. Amorphous thin films of molybdenum oxide are used as electrochemical sensors for iodide ions [11], whereas the crystalline ones find applications for carbon monoxide sensors [12]. $MoSe_2$ absorbs light in the visible and near-IR regions and exhibits an inherent resistive nature to photocorrosion [13]. Complex $MoSe_2|MoO_2$ systems have also gained application in the fuel elements [14], and electrocatalysis [7, 15], while amorphous MoO_yS_x films—in lithium battery cells [16].

Electrodeposition of molybdenum oxide films has been investigated before by several groups. Different methods were applied for the preparation of molybdenum oxides thin films. The precursors were usually MoO_4^{2-} [17, 18], iso- and peroxo-polymolybdate [19–21], ammonium paramolybdate [22], and polymolybdophosphate [23] aqueous solutions. Hydrated amorphous molybdenum (IV) oxides on fluorine-doped SnO_2 [6] and highly oriented pyrolitic graphite [17] surfaces were electrodeposited from aqueous alkaline solutions containing MoO_4^{2-} as the precursor. Alternatively, the non-stoichiometric mixed-valence molybdenum (VI and V)

oxides were grown on glassy carbon surface from aqueous acidic solutions of sodium molybdate [11].

McEvoy and Stevenson [20, 24] reported cathodic electrodeposition of molybdenum oxide on indium doped SnO_2 (ITO) electrode from aqueous acidic solution of isopolymolibdates and peroxo-polymolibdates and studied reaction mechanisms using different characterization tools. Deposition at specific applied potentials allowed formation of molybdenum oxides with varying composition, such as Mo_3O_8, Mo_2O_5, and $Mo_{3-x}O_{8-x}(OH)_x{\cdot}xH_2O$. In contrast, Banica et al. [21] reported the formation of a stable $MoO_2{\cdot}xH_2O$ film on Pt support from aqueous acidic peroxo-polymolybdate solutions. A mixture of non-hydrated Mo_2O_5 with tetravalent $MoO(OH)_2$ was deposited from aqueous ammonium paramolybdate solutions [22]. Non-stoichiometric $Mo_4O_{11}{\cdot}nH_2O$ has also been successfully obtained via electrodeposition on stainless steel [25]. In this compound molybdenum is pentavalent, and, therefore, can be regarded as a double Mo_2O_5 molecule coordinated via one oxygen atom. From literature analysis presented above, it is evident that the properties and composition of electrolytic molybdenum oxide films are closely related to electrolyte composition [17, 20, 22], electrolyte pH [22], and applied potential [20, 22, 24].

In this work, we used electrodeposition techniques to obtain layered molybdenum oxide films for potential application in photocatalysis and optical technologies. Electrodeposition was performed in freshly prepared 0.22 M sodium citrate ($C_6H_5Na_3O_7$) solution (pH 8.3), and the sodium molybdate was used as a precursor. Cyclic voltammetric study was used to determine the deposition potential range for obtaining the thin films on Se|SnO_2|glass surface. To the best of our knowledge, the interaction between a selenium support and the electrodeposited film is reported for the first time. The compositional, structural, and optical properties of as deposited thin films are also presented. The photocatalytic properties of these thin films are the subject of a further study.

Experimental methods

Electrochemical experiments and cyclic voltammetry The electrochemical measurements were performed in a conventional three-electrode JCE-2 cell, using a computer-controlled Autolab PGSTAT12 (Ecochem, the Netherlands) potentiostat/galvanostat. The GPES® 4.9 software was used for collection and treatment of experimental data. Cyclic voltammetric measurements were carried out by starting scan towards the negative potential. The potential sweep rate was 50 mV/s. The electrolyte solution was 0.2 M Na_2MoO_4 in 0.22 M sodium citrate and pH value of 8.3. All solutions were prepared using doubly distilled water and analytical grade reagents. SeO_2 (>99%, Reachim, Russia), $Na_2MoO_4{\cdot}2H_2O$ (>99%, Sigma-Aldrich, Germany), and sodium citrate ($C_6H_5Na_3O_7{\cdot}2H_2O$; >99%, Lachema, Czech Republic) were used as received. pH of the solutions was adjusted by adding 1 M H_2SO_4 or 6 M NaOH solutions. Only freshly prepared solutions were used for measurements and were not deaerated during the experiments. All measurements were carried out at 293 K. The counter-electrode was a platinum spiral with an active area of 12.5 cm^2. The reference electrode was a Ag|AgCl, $KCl_{(sat)}$ electrode. Through the paper, all potential values are referred to this reference electrode. The commercially available (Nippon Sheet Glass Co, Japan) SnO_2-coated glass plates, prepared using spray pyrolysis technique, were used as the working electrodes (further referred to as SnO_2|glass electrode). The thickness of the SnO_2 layer was ~1 μm. The presence and crystallinity of the SnO_2 films was confirmed by the XRD analysis. The results confirmed the tetragonal structure and the polycrystalline nature of the SnO_2 layers.

The SnO_2|glass electrode was fixed in a stainless steel cylindrical holder and the electrical contact was realized using a copper stick. The geometrical area of the SnO_2|glass electrode was 4.5 cm^2. Before experiments, the SnO_2-coated glass electrodes were cleaned with acetone, followed by 0.1 M HNO_3 solution, and finally rinsed with the distilled water.

Se|SnO₂|glass electrode preparation A thin selenium film was initially deposited on the SnO_2|glass electrode using a 0.01 M H_2SeO_3 solution and 0.22 M sodium citrate as a supporting electrolyte (pH 5.76). Electrodeposition was performed applying cathodic current of 1.0 mA for 10 min. Electrolysis temperature was 293 K. Resulting Se films have been rinsed with double distilled water. The thickness of Se film was about 90 nm, as determined using X-ray photoelectron spectroscopy (XPS) analysis.

XPS measurements A custom-designed Kratos Axis Ultra X-ray photoelectron spectroscopy system was used to determine the elemental composition of the thin films. The experimental setup for reactions and analysis has been described in detail before [26]. Briefly, the surface analysis chamber is equipped with monochromatic radiation at 1,486.6 eV from an aluminum K_α source using a 500 mm Rowland circle silicon single crystal monochromator. The X-ray gun was operated using a 15 mA emission current at an accelerating voltage of 15 kV. Low energy electrons were used for charge compensation to neutralize the sample. Spectra were acquired in the region of interest using the following experimental parameters: 20 to 40 eV energy window, pass energy of 80 eV, dwell of 0.1 s, and sweep time of 30 s. One sweep was used to acquire all the

regions. Spectra were acquired from 110 μm circular area. The absolute energy scale was calibrated to the Cu $2p_{2/3}$ peak binding energy of 932.6 eV using an etched copper plate. A Shirley-type background was subtracted from each spectrum to account for inelastically scattered electrons that contribute to the broad background. CasaXPS software was used to process the XPS data [27]. Transmission-corrected relative sensitivity factor values from the Kratos library were used for elemental quantification. Since common C1s energy calibration cannot be done in depth profiling experiments, all spectra were calibrated to the O1s value of 530.5 eV. Peak at 530.5 eV is due to the most abundant species present in these samples, MoO_2.

In depth profiling experiments, an argon ion beam produced in an argon gun operating at 4.8 kV and 15 mA emission current was used. Beam raster size was 1.5 mm, whereas beam current was ~0.5 μA. Electrons were sampled from 110 μm diameter area. Etch rate was determined against a known thickness TaO_2 layer on Ta metal and was found to be ~0.3 Å/s.

AFM measurements Atomic force microscopy was performed using the Asylum Research MFP-3D AFM instrument. Alternating current mode was used in all experiments. Topography, amplitude, and phase images were acquired simultaneously using 512 pixels per line resolution and 512 lines. A rectangular silicon cantilevers (125 μm length) from MikroMasch were used (NSC15/Al BS, backside of probe aluminum-coated, resonant frequency between 265 and 400 kHz and typical force constant of 40 N/m). Scan rates were 1 Hz.

UV–VIS measurements UV–VIS spectrometry analysis was carried out to investigate the optical properties of the Mo–Se thin films. UV–VIS spectra were recorded using a UV/VIS Spectronic Genesis spectrophotometer (Perkin Elmer Spectrum GX, USA) in the range of 350–1,100 nm. The optical absorption spectra of thin films was taken using an identical transparent tin oxide-coated glass plate as a reference, and the values of the optical absorption coefficient α were not corrected for the reflectance from the film surface. The optical band gap energy, E_{og}, was obtained by studying the absorption edge behavior.

Results and discussion

Cyclic voltammetry

Cyclic voltammetry was used to monitor the electrochemical reactions in order to find a suitable deposition potential. Before each scan, the potential was monitored until attaining the steady-state value. First, electrochemical properties of $Se|SnO_2|$glass electrode in 0.22 M sodium citrate solution were determined. Cyclic voltammogram of $Se|SnO_2|$glass electrode in +1.2 to −1.2 V potential range in 0.2 M sodium citrate solution is shown in Fig. 1. Two characteristic cathodic potential ranges are observed: a wave c_1 and an abrupt increase of current c_2. The cathodic wave c_1 is associated with the reduction of selenium according to the reaction [28, 29]:

$$Se + H^+ + 2e^- \rightarrow HSe^-_{(ads)} \quad , E^\circ = -0.449V \tag{1}$$

A significant current flow at −0.8 V is related to the hydrogen evolution reaction (HER) [29, 30]. When potential was reversed at −1.2 V and scanned towards the positive values, no anodic features were observed in curve.

The addition of 0.2 M Na_2MoO_4 solution to the 0.22 M sodium citrate caused significant changes in CV profile (Fig. 1). Higher deposition currents were observed and a new reduction peak c_3 centered at −0.55 V became prominent. The peak c_3 is positioned in the potential domain where the reaction (1) occurs. However, peak potential shifted by 140 mV towards negative values with respect to the half wave potential ($E_{1/2}$) observed for a pure sodium citrate solution. Two competitive factors can be responsible for this phenomenon: (1) slow electron transfer kinetics through the selenium layer towards MoO_4^{2-} species and (2) formation of passive film on electrode surface in initial stage of electrodeposition.

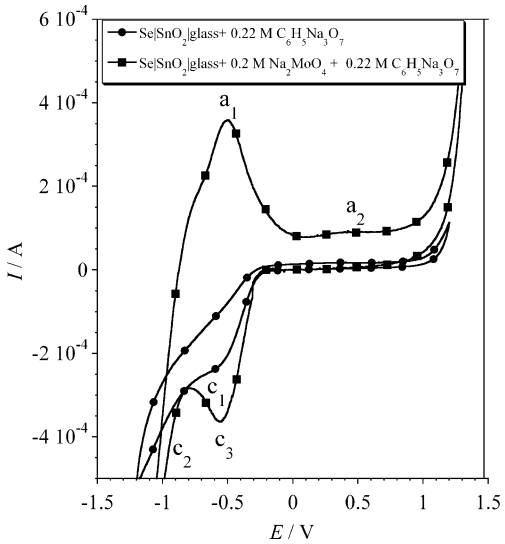

Fig. 1 Cyclic voltammograms of $Se|SnO_2|$glass electrode in 0.22 M $C_6H_5Na_3O_7$ and 0.2 M Na_2MoO_4+0.22 M $C_6H_5Na_3O_7$ solution at potential sweep rate of 50 mV/s. Characteristic cathodic and anodic waves are noted with corresponding letters and discussed in the text

During reduction of MoO_4^{2-} ions two additional parallel reactions can proceed simultaneously:

$$2MoO_4^{2-} + 3H_2O + 2e^- \rightarrow Mo_2O_5 + 6OH^- \quad E^\circ = +0.552V \tag{2}$$

$$MoO_4^{2-} + 2H_2O + 2e^- \rightarrow MoO_2 + 4OH^- \quad E^\circ = +0.404V \tag{3}$$

Although the standard potentials of these reactions are positive, the actual molybdenum oxide formation occurs with a significant value of overpotential [10].

The Pourbaix diagram [31] for molybdenum revealed the thermodynamically stable MoO_2 in the potential range of −0.5 to −0.8 V at pH 8.3, while Mo_2O_5 oxide was reported to be stable in acidic and neutral solutions within −0.3 to −0.8 V potential range [22, 32].

Considering the thermodynamic stability of different molybdenum oxides and conclusions made by different authors [6, 17, 22], the cathodic current c_3 can be related with the reduction of MoO_4^{2-} ions to Mo(IV) with formation of MoO_2 (reaction 3).

We propose that the reduction of MoO_4^{2-} ions is hindering the destruction of selenium layer. The cathodic current drop around −0.5 V (Fig. 1) confirms formation of the electrically passive film in the initial stages of the scan. Additionally, reaction (3) causes a local increase in OH^- concentration near the electrode surface. Consequently, the rate of reaction (1) should decrease, and HSe^- is being formed at more negative potentials.

In order to analyze oxidation processes of these films, cyclic voltammograms between potentials of +1.3 to −0.8 V were recorded. Fig. 2 shows the effect of the cathodic scan limits on the reverse scan towards positive potential. On the forward cathodic scan up to the potential values of wave c_3 (−0.6 and −0.8 V, respectively), no associated anodic peaks were recorded in the reverse scan. The repeated potential cycles showed only the irreversible current behavior.

The cathodic current c_2 (Fig. 1) is larger than that observed for HER on Se|SnO_2|glass surface. According to Pourbaix diagram [31], two competitive reactions are possible over this potential domain:

$$MoO_2 + 2H_2O + 4e^- \rightarrow Mo + 4OH^- \quad , E^\circ = -1.199V \tag{4}$$

and MoO_4^{2-} reduction to Mo(0) by reaction:

$$MoO_4^{2-} + 4H_2O + 6e^- \rightarrow Mo + 8OH^- \quad , E^\circ = -1.226V \tag{5}$$

It is thermodynamically favorable for molybdenum metal to spontaneously react with H_2O to produce $MoO_x{\cdot}yH_2O$ with hydrogen evolution [17, 31, 32].

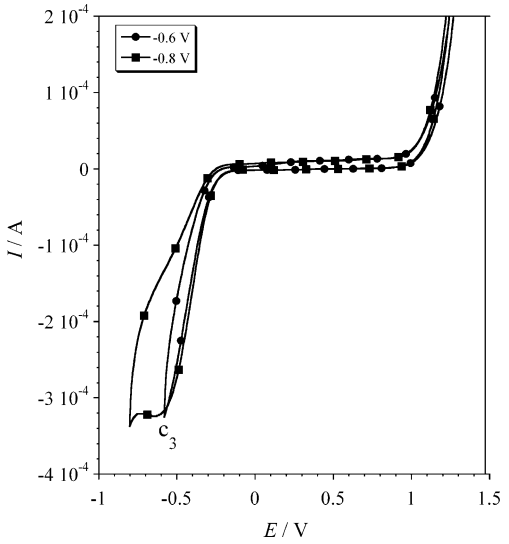

Fig. 2 Cyclic voltammograms of Se|SnO_2|glass electrode recorded for negative potential limits of −0.6 and −0.8 V in 0.22 M $C_6H_5Na_3O_7$+ 0.2 M Na_2MoO_4 electrolyte at potential sweep rate of 50 mV/s. Characteristic cathodic and anodic waves are noted with corresponding letters and discussed in the text

In this potential range, the interaction of the cathode surface with hydrated molybdenum oxide and adsorbed hydrogen caused destruction of selenium layer. As mentioned above, the formation of Mo(IV) oxides suppresses Se reduction (reaction 1) and shifts the formation of HSe^- towards more negative potentials. This way hydrated molybdenum oxide formed in interaction with selenium layer may lose molecular water, and the overall cathodic process can be described according to reaction:

$$MoO_2 \cdot xH_2O + e^- \rightarrow MoO_2 + xH_{ads} + xOH^- \tag{6}$$

Adsorbed hydrogen atoms reduce selenium layer:

$$2H_{ads} + Se \rightarrow H_2Se \tag{7}$$

In turn, the direct reduction of selenium to Se^{2-} ions can occur:

$$Se + 2e^- \rightarrow Se^{2-} \quad E^\circ = -1.199V \tag{8}$$

The cyclic voltammograms presented in Figs. 2 and 3 clearly show that cathodic current c_2 is associated with the appearance of the broad peak a_1 at E_p=−0.48 V and a weak feature a_2 on the reverse anodic scan. Moreover, anodic peaks a_1 and a_2 were only observed on anodic curve when potential scan limit of −1.0 V was applied (Fig. 3). Shift of cathodic limits to more negative potential values causes the increase of anodic peak a_1 while anodic peak a_2 potential shifts towards the negative direction. In addition, peak a_2 reaches maximum and vanishes when more negative potentials were applied.

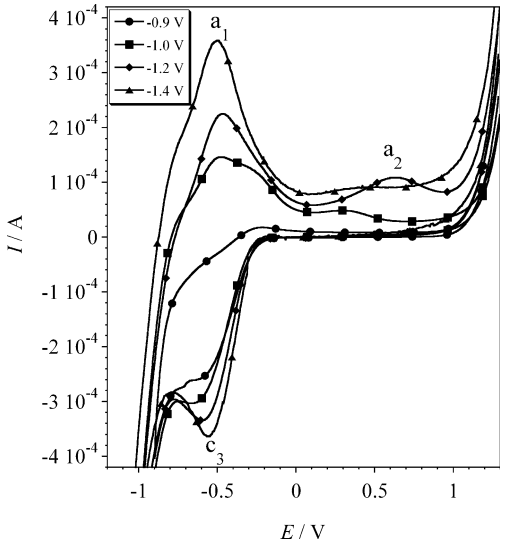

Fig. 3 Cyclic voltammograms of Se|SnO_2|glass electrode recorded for negative potential limits of −0.9, −1.1, −1.2, and −1.4 V in 0.22 M $C_6H_5Na_3O_7$+0.2 M Na_2MoO_4 electrolyte at potential sweep rate of 50 mV/s. Characteristic cathodic and anodic waves are noted with corresponding letters and discussed in the text

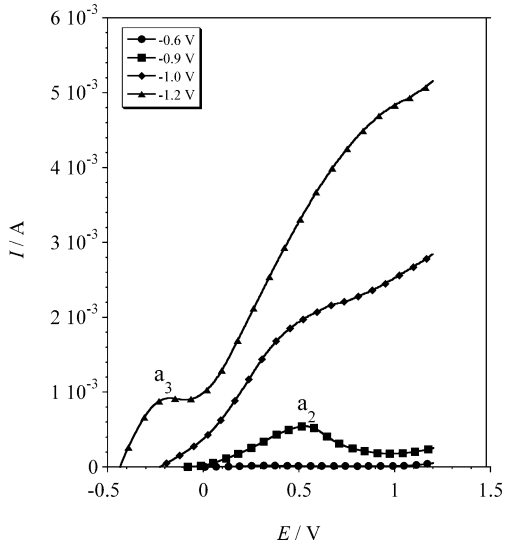

Fig. 4 Anodic linear sweep voltammetry (ALSV) curves corresponding to the cathodic linear sweep performed in 0.2 M Na_2MoO_4+0.22 M $C_6H_5Na_3O_7$ solution, both performed at potential sweep rate of 50 mV/s. Cathodic limits used were −0.6, −0.9, −1.0, and −1.2 V. Characteristic anodic waves are noted with corresponding letters and discussed in the text

Anodic peak a_1 was observed in the potential range that corresponds to Se^{2-} ions oxidation to elemental selenium [30]. This selenium during anodic scan oxidizes at potentials more positive than +0.9 V [28, 29].

Two combined Linear Sweep Voltammetries were applied in order to determine the nature of the anodic wave a_2 and to avoid interaction between species formed on the electrode surface and species in solution. First, the negative potential sweep was performed scanning from E=−0.09 V towards the selected negative potential limits (cathodic linear sweep voltammetry). When cathodic limit was reached, the potential was held for 2 min in order to increase the amount of the deposited species. After the electrolysis, electrode was removed from electrolyte solution, subsequently placed in to 0.22 M sodium citrate solution (pH 8.3), and the positive scan was performed.

When cathodic potential scan was performed towards −0.6 V and, after subsequent electrolysis, no anodic dissolution peaks were recorded on anodic linear sweep voltammetry (ALSV) curve (Fig. 4). The absence of any appreciable anodic current indicates that the film is hardly oxidizable.

When potential scan was performed towards −0.9 V and after subsequent electrolysis, a broad small anodic peak a_2 with a maximum at +0.55 V can be observed in ALSV curves (Fig. 4).

Shift of the cathodic scan limits to more negative potential values leads to a new anodic feature labeled a_3 with wave a_2 also increasing. These processes partially overlap. The change of scan rate also does not result in their resolution.

The absence of the anodic peak a_1 in ALSV (Figs. 2 and 4) indicates that Se^{2-} ions, being negatively charged under prolonged deposition conditions, diffuse away from electrode surface.

Analysis of LASV curves revealed that films deposited at potentials negative then −0.9 V are less resistive to oxidation than those obtained at −0.9 V. The detection of several anodic peaks can be attributed to the oxidation via different intermediate phase. No attempt was made to analyze oxidation products and identify anodic a_2 and a_3 peaks.

Chronoamperometric studies

The current transient was performed in 0.22 M $C_6H_5Na_3O_7$+ 0.2 M Na_2MoO_4 solution (pH 8.3) at 293 K and constant potentials values of: −0.7, −0.8, −0.9, −1.0, and −1.2 V.

Table 1 Electrodeposition conditions and sample numbering

Number	Sample	Electrodeposition conditions	
		Deposition time (min)	Deposition potential (V)
1	MoSe9	10	−0.9
2	MoSe1	1	−1.0
3	MoSe2	5	−1.0
4	MoSe3	10	−1.0
5	MoSe4	30	−1.0
6	MoSe5	1	−1.2
7	MoSe6	5	−1.2
8	MoSe7	10	−1.2
9	MoSe8	30	−1.2

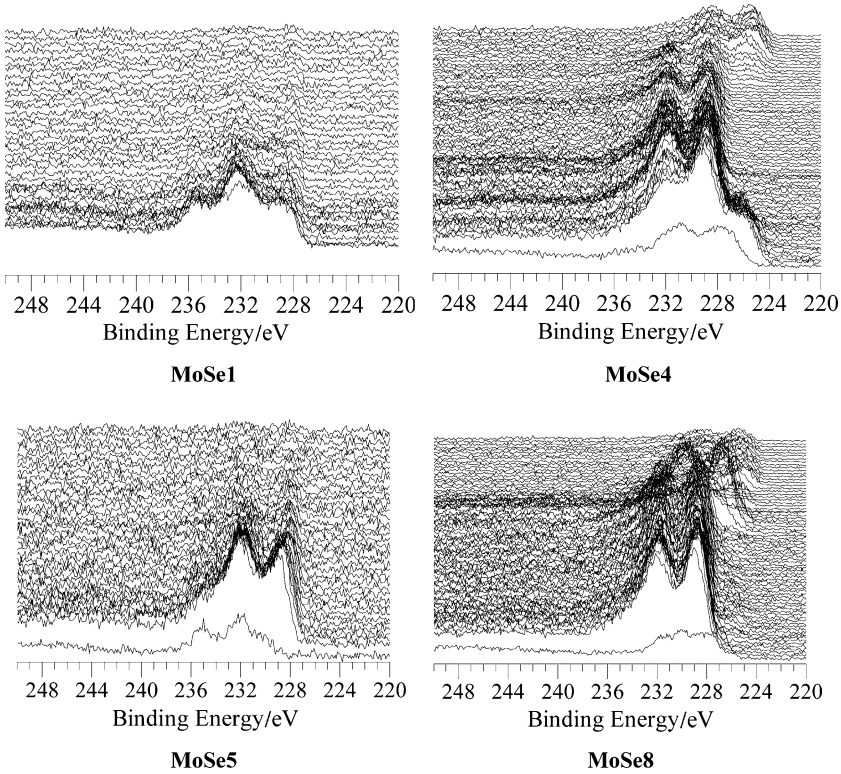

Fig. 5 Representative Mo3d spectra of MoSe1, MoSe4, MoSe5, and MoSe8 thin film depth profiles. Spectra shown were acquired within the 1,110 s depth profiling interval for MoSe1 and MoSe5 and 9,060 s depth profiling interval for MoSe4 and MoSe8 thin films

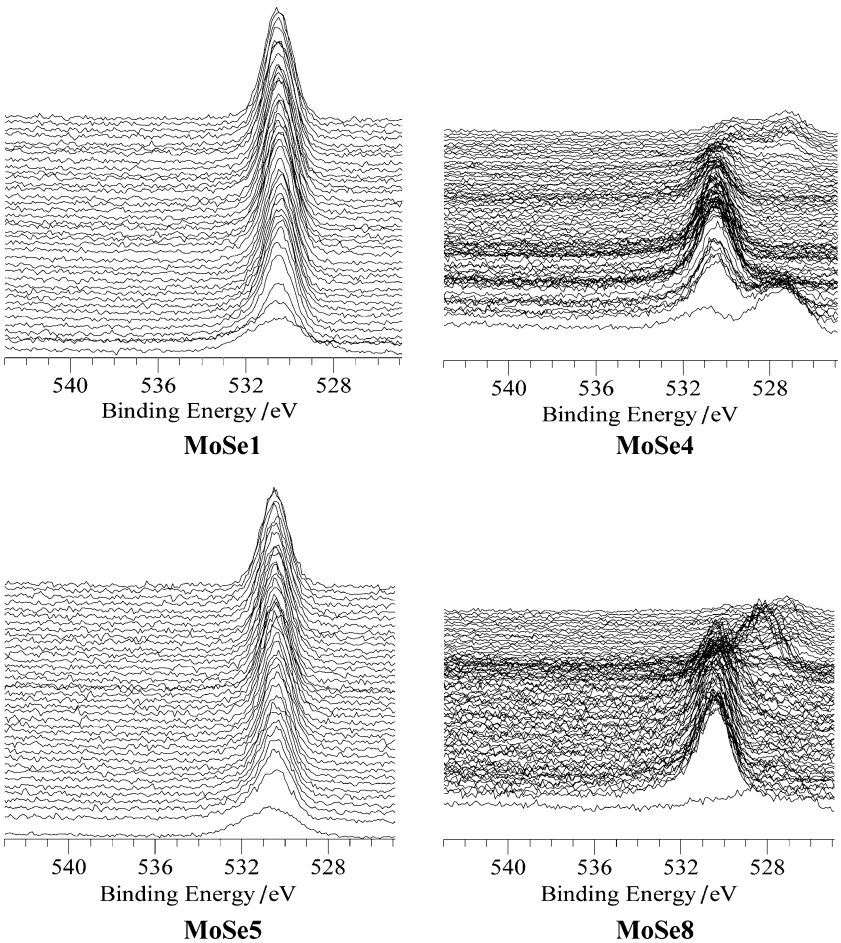

Fig. 6 Representative O1s spectra of MoSe1, MoSe4, MoSe5, and MoSe8 thin film depth profiles. Spectra shown were acquired within the 1,110 s depth profiling interval for MoSe1 and MoSe5 and 9,060 s depth profiling interval for MoSe4 and MoSe8 thin films

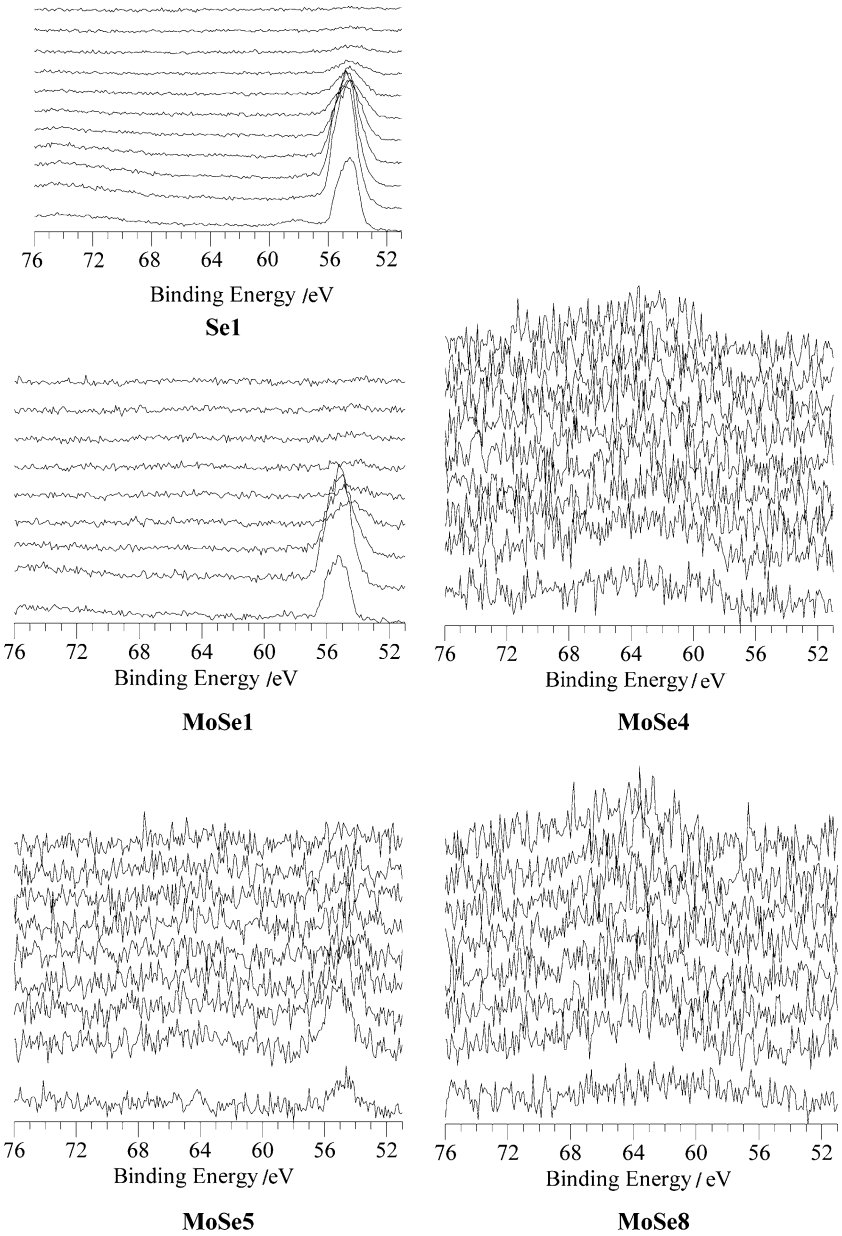

Fig. 7 Representative Se3d spectra of MoSe1, MoSe4, MoSe5, and MoSe8 thin film depth profiles. Spectra shown were acquired within the 240 s depth profiling interval for all films. Bare selenium thin film representative Se3d spectra of the 1,200 s interval depth profile is also shown

At −0.7 and −0.8 V potentials, current initially sharply increases, passes through a maximum value, and in 30 s, gradually decreases to a negligible value. Thus, at present experimental conditions, it was impossible to obtain appreciable amount of the deposit. The impossibility of depositing thicker coatings may be caused by the formation of the electrically inactive film layer in the initial stages and more negative deposition potential should be applied to overcome this passivity effect.

Different samples (Table 1) were prepared in order to elucidate the influence of deposition time and deposition potential on thin films structural composition. Deposition current was monitored in each experiment. Electrolysis conditions and sample numbering are listed in Table 1.

Regardless of the deposition potential as-deposited thin films were well-adhered to the substrate and transparent, brown in color. No visible defects such as cracks, voids, porosity, or loose particles were found.

After deposition, thin films were rinsed with acetone and analyzed with XPS.

X-ray photoelectron spectroscopy analysis

XPS analysis was performed in order to (a) establish the speciation of the Mo and Se compounds formed during the thin film deposition and (b) obtain the depth-related elemental information. Mo3d spectra of MoSe1, MoSe4, MoSe5, and MoSe8 thin film depth profiles are shown in

Table 2 XPS peak assignments of $Mo3d_{5/2}$ and Se3d transition in deposited films

Region	Compound or assigned species	Binding energy (eV)	
		This work[a]	Literature reference[b]
$Mo3d_{3/2}$	MoO_3	232.2	232.6
	MoO_2	229.3	229.1
Se3d	Se–Mo	55.2	N/A

N/A literature references were not found

[a] Calibrated to the O1s peak at 530.4 eV

[b] Clayton et al. [22] calibrated to C1s at 284.6 eV

Fig. 5, whereas O1s and Se3d spectra of the same depth profiles are shown in Figs. 6 and 7, respectively.

Spectra shown were acquired within the 1,110 s depth profiling interval for MoSe1 and MoSe5 and 9,060 s depth profiling interval for MoSe4 and MoSe8 thin films in Fig. 5 and within the 240 s depth profiling interval for all films. Se1 thin film representative Se3d spectra of the 1,200 s interval depth profile is also shown in Fig. 7. XPS data of MoSe1, MoSe4, MoSe5, and MoSe8 films is shown here as it represents that of all films synthesized and analyzed. Representative sample labeling and electrodeposition conditions are shown in Table 1, whereas representative Mo3d and Se3d peak assignments are shown in Table 2. Several peaks were observed in Mo3d spectra for all thin films investigated here. As a useful trend, molybdenum species detected did not change with depth in samples deposited at shorter deposition times (MoSe1, MoSe2, and MoSe3), as well as MoSe5 and MoSe6. These all had characteristic Mo3d doublets with $Mo3d_{5/2}$ peaks located at 232.2 and 229.3 eV. $Mo3d_{5/2}$ peak at 232.2 eV rapidly decreased in intensity with film thickness. It has previously been assigned to fully oxidized Mo(VI) species in MoO_3 [33].

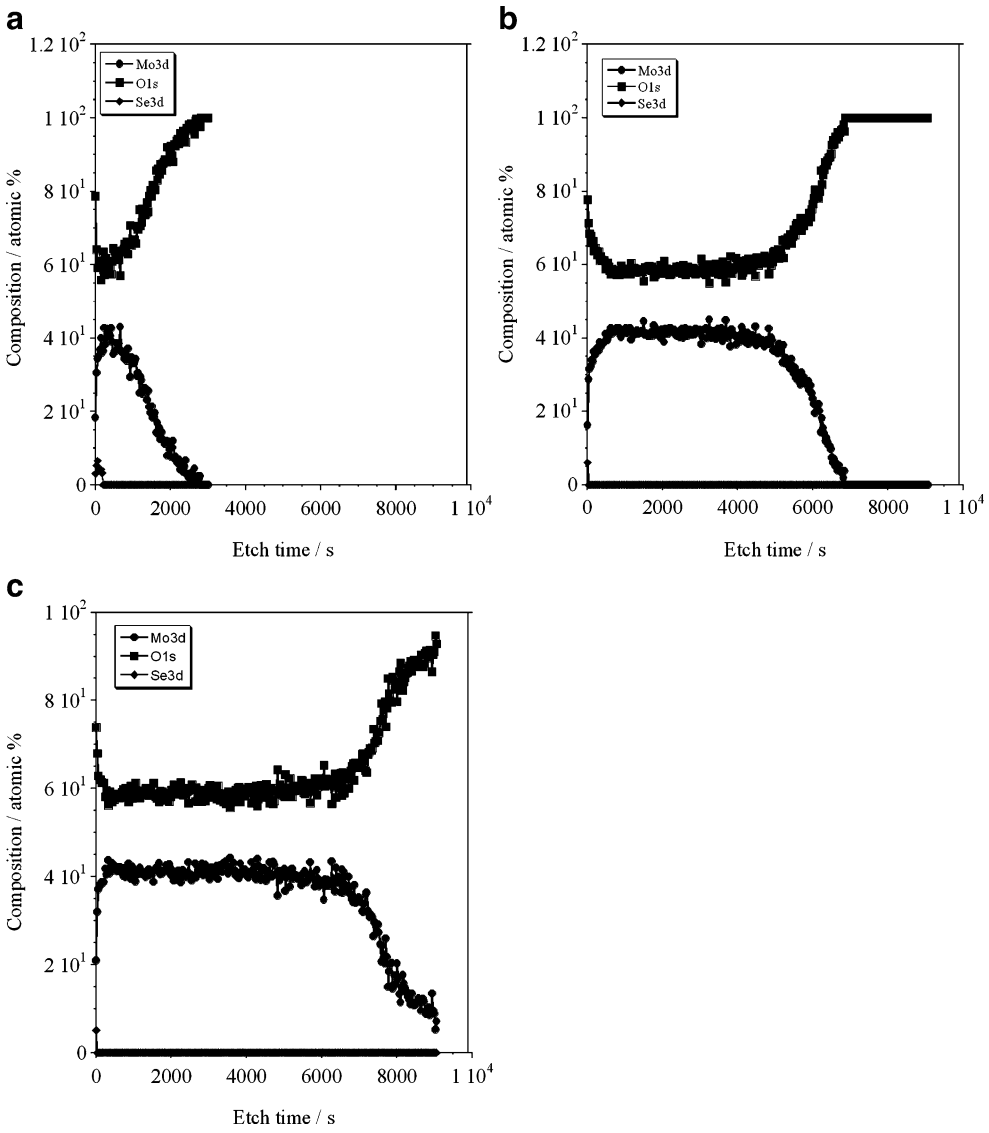

Fig. 8 XPS depth profile determined elemental composition of Mo–Se thin films at deposition voltages of −0.9, −1.0, and −1.2 V. Total composition is shown for MoSe9, MoSe3, and MoSe7 films in terms of Mo3d, O1s, and Se3d regions

Table 3 XPS depth profile determined composition of films after 10 min of deposition at varying potential

−0.9V (MoSe9)		−1.0V (MoSe3)		−1.2V (MoSe7)	
Etch time (s)	Composition	Etch time (s)	Composition	Etch time (s)	Composition
0–60	MoO_3, MoO_2, Se	0–210	MoO_3, MoO_2	0–9,060	MoO_2
60–300	MoO_2, Se				
300–2,820	MoO_2	210–6,840	MoO_2		

This species can arise from the thin MoSe film oxidation in the atmosphere.

A predominant species in all spectra with $Mo3d_{5/2}$ peak located at 229.3 eV was assigned to Mo(IV) in MoO_2 [22]. This was the majority product found in all MoSe films synthesized after surface layers were removed. Depending on the deposition time, Mo(IV) species could be found after 8,280 s of depth profiling in MoSe4 and 5,070 s in MoSe8, corresponding to ~250 and ~150 nm, respectively.

A third distinct molybdenum species was observed in MoSe4, MoSe7, and MoSe8 samples with $Mo3d_{5/2}$ peak located at 225.4 eV. A distinct location of this layer was below the Mo(IV) layer in the three films mentioned above (MoSe4, MoSe7, and MoSe8), e.g., only in thicker films with longest deposition times. A peak at 226.1 eV has previously been assigned to Mo in metallic state [34]. However, most of the literature references showed that metallic molybdenum has $Mo3d_{5/2}$ peak located at

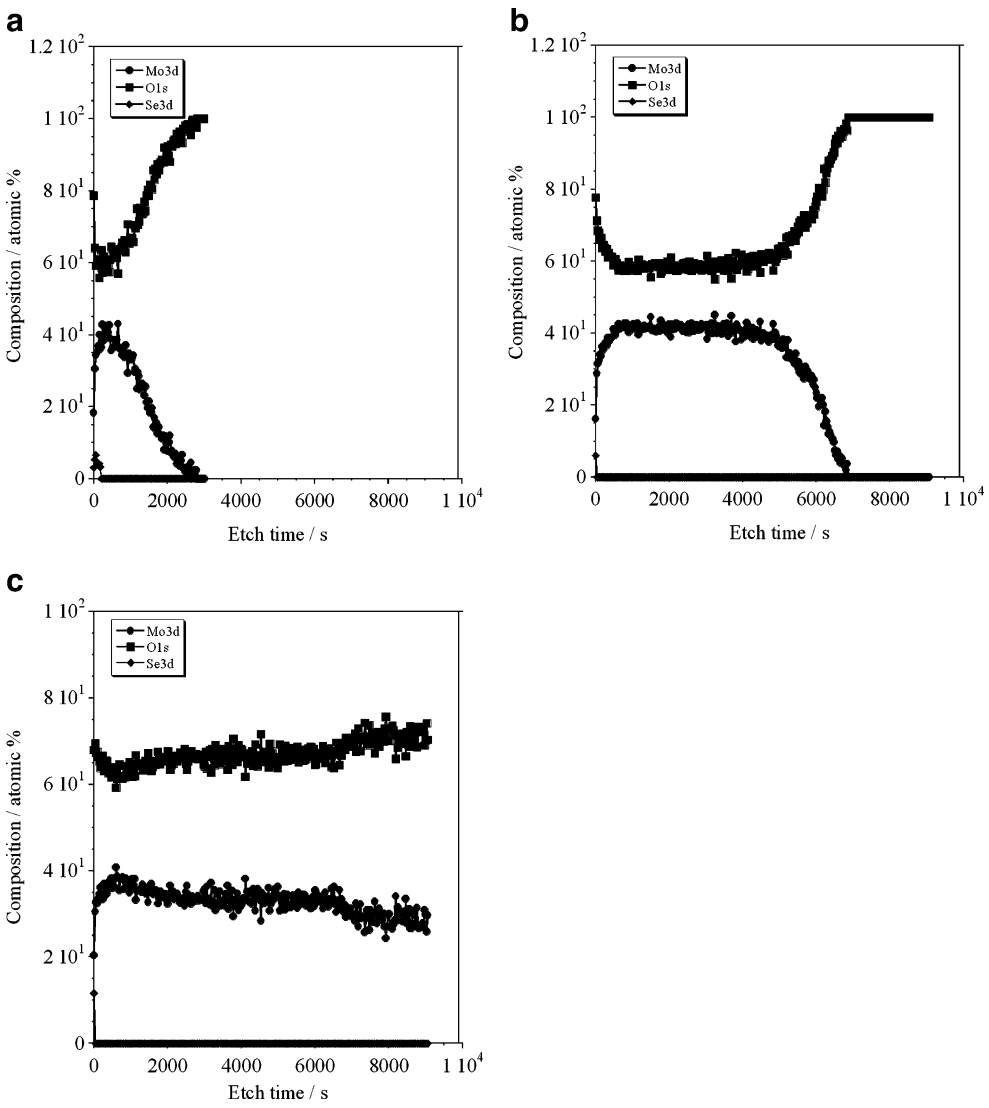

Fig. 9 XPS depth profile determined elemental composition of thin films at constant deposition voltage of −1.0 V as a function of deposition time. Total composition is shown for MoSe2, MoSe3, and MoSe4 films deposited for 5, 10, and 30 min, respectively, in terms of Mo3d, O1s, and Se3d regions

Table 4 XPS depth profile determined composition of Mo–Se films at constant deposition potential of −1.0 V

5min (MoSe2)		10min (MoSe3)		30min (MoSe4)	
Etch time (s)	Composition	Etch time (s)	Composition	Etch time (s)	Composition
0–1,140	MoO_3, MoO_2, Se	0–210	MoO_3, MoO_2	0–9,060	MoO_2
1,140–4,320	MoO_3, MoO_2	210–6,840	MoO_2		

228.0 eV [33, 35]. The $Mo3d_{5/2}$ binding energy shift from 229.3 to 225.4 eV coincides with a gradual O1s peak shift from 530.5 to 527.3 eV, as well as Na1s peak shift by ~3 eV (not shown) implying change in electric properties of the sample, rather than a change in the molybdenum oxidation state. To eliminate the possibility of the sample differential charging, sample was "floated," e.g., direct contact with ground was removed. The same peak shift was observed thus confirming change in electric properties of the sample. Most importantly, this shift was strongly

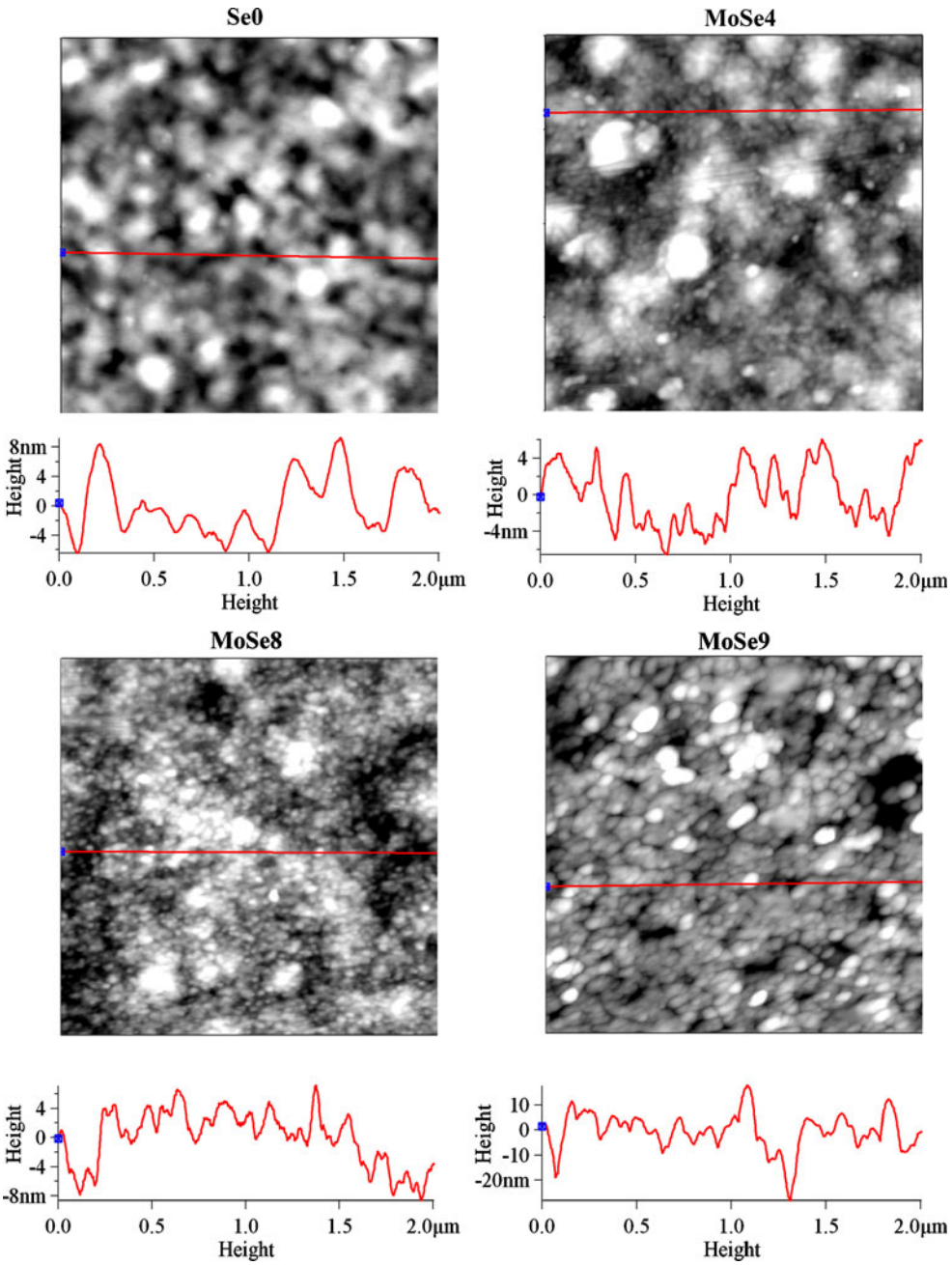

Fig. 10 Representative AFM images of Se1, MoSe4, MoSe8, and MoSe9 films. The image sizes are 2 μm. *Line scans* for each image are also shown *underneath*

correlated with decrease in of Sn3p peak intensity. In MoSe4, MoSe7, and MoSe8, Sn3p peak was negligible or completely absent throughout all of the depth profiling experiment. Change in Sn concentration on the sample has affected its electric properties thus affecting the equilibrium between the flux of outgoing photoelectrons and charge neutralizer electrons.

O1s spectra of MoSe1, MoSe4, MoSe5, and MoSe8 thin films are shown in Fig. 6. Two main peaks can be seen in all O1s spectra. A peak located at 530.5 eV can be attributed to Mo–O bond. This peak was also pronounced in MoSe4 and MoSe8, together with the peak ~528 eV. The latter appeared only in deeper layers and always coincided with the appearance of $Mo3d_{5/2}$ 225.4 eV peak (MoSe4, MoSe7, and MoSe8). The nature of this peak can be explained by the change in electric properties of the samples with the removal of Sn layer (vide supra). Moreover, it is only partially related to any of the molybdenum species. This can be illustrated using MoSe7 film, where after 9,060 s of etching Mo3d signal almost disappeared, whereas O1s peak at ~528 eV was present with ~40% abundance. While O1s in molybdenum oxides is commonly found around 530 eV, atomic oxygen dissociated on clean metal surfaces upon adsorption with O1s peak at 529.5 eV [36] and lattice O^{2-} species at 529.0 eV in mixed $MoO_x|(LaCoO_3+Co_3O_4)$ catalysts [37]. This confirms the fact that O1s peak shift to 528 eV is due to the electric phenomena of the glass, rather than change in speciation. Here, we propose that the main peak at 530.5 eV is due to both molybdenum oxide and hydroxide species.

Se3d spectra of Se1, MoSe1, MoSe4, MoSe5, and MoSe8 thin films are shown in Fig. 7. Surprisingly, selenium was only detected in small amounts on the surface of the films and not underneath the molybdenum layer (where molybdenum layer was fully removed via depth profiling). Small amounts of selenium were detected on MoSe1 and MoSe5 thin films fully disappearing after 120 s of depth profiling, corresponding to 3.6 nm thickness. MoSe4 and MoSe8 films showed no Se3d signal throughout all profiling. Measured Se3d binding energy of Se in Se1 film is 54.6 eV, lower than that in MoSe1 of 55.2 eV. This shift in binding energy can be assigned to two different species of selenium: Se(0) in Se1 and $MoSe_2$ in MoSe1 film.

The effect of the deposition potential on quantitative depth profile information can be seen in Fig. 8 a, b, and c in terms of Mo3d, O1s, and Se3d regions. Quantitative description of the depth profiles is summarized in Table 3. Thin films MoSe9, MoSe3, and MoSe7 represent deposition potentials of −0.9, −1.0 and −1.2 V, respectively. Data in Fig. 8 shows an increasing thickness of molybdenum oxide films with an increase in deposition potential. For MoSe9, amount of molybdenum in the deposited film is ~40% after ~500 s of etching and then gradually decreases to zero after 3,000 s of etching. MoSe3 shows a steady-state concentration of Mo in the film of ~40% to ~5,000 s of etching, where its concentration starts gradually decreasing until no Mo is present after 7,000 s of etching. Finally, MoSe7 shows a constant molybdenum concentration of 40% which decreases to zero after 7,000 s of etching. This confirms that the thickness of Mo film formed increases with the deposition potential.

The effect of the deposition time on the quantitative depth profile information can be seen in Fig. 9 a, b, and c in terms of Mo3d, O1s, and Se3d regions for MoSe2, MoSe3, and MoSe4 films. Quantitative description of these depth profiles is summarized in Table 4. These thin films with deposition times of 5, 10, and 30 min. Data shows an increasing thickness of molybdenum oxide films with an increase in deposition time. For MoSe2, amount of molybdenum in the deposited film is ~30% after ~500 s of etching and then gradually decreases to zero after 4,000 s of etching. MoSe3 shows a steady-state concentration of Mo in the film of ~40% to ~5,000 s of etching, where its concentration starts gradually decreasing until no molybdenum is present after 7,000 s of etching. Finally, MoSe4 shows a constant concentration between 30% and 40% even after the 9,000 s of etching. This shows that the thickness of Mo film formed increases with the deposition time at constant deposition potential.

Atomic force microscopy

Representative AFM images of Se1, MoSe4, MoSe8, and MoSe9 films are shown in Fig. 10. All image sizes shown

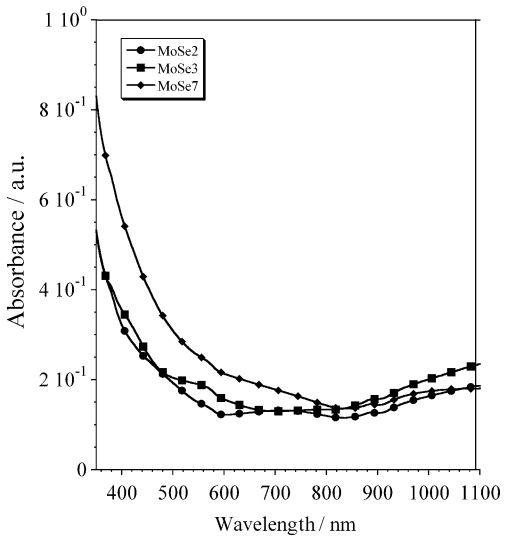

Fig. 11 UV–VIS spectra of MoSe2, MoSe3, and MoSe7 thin films

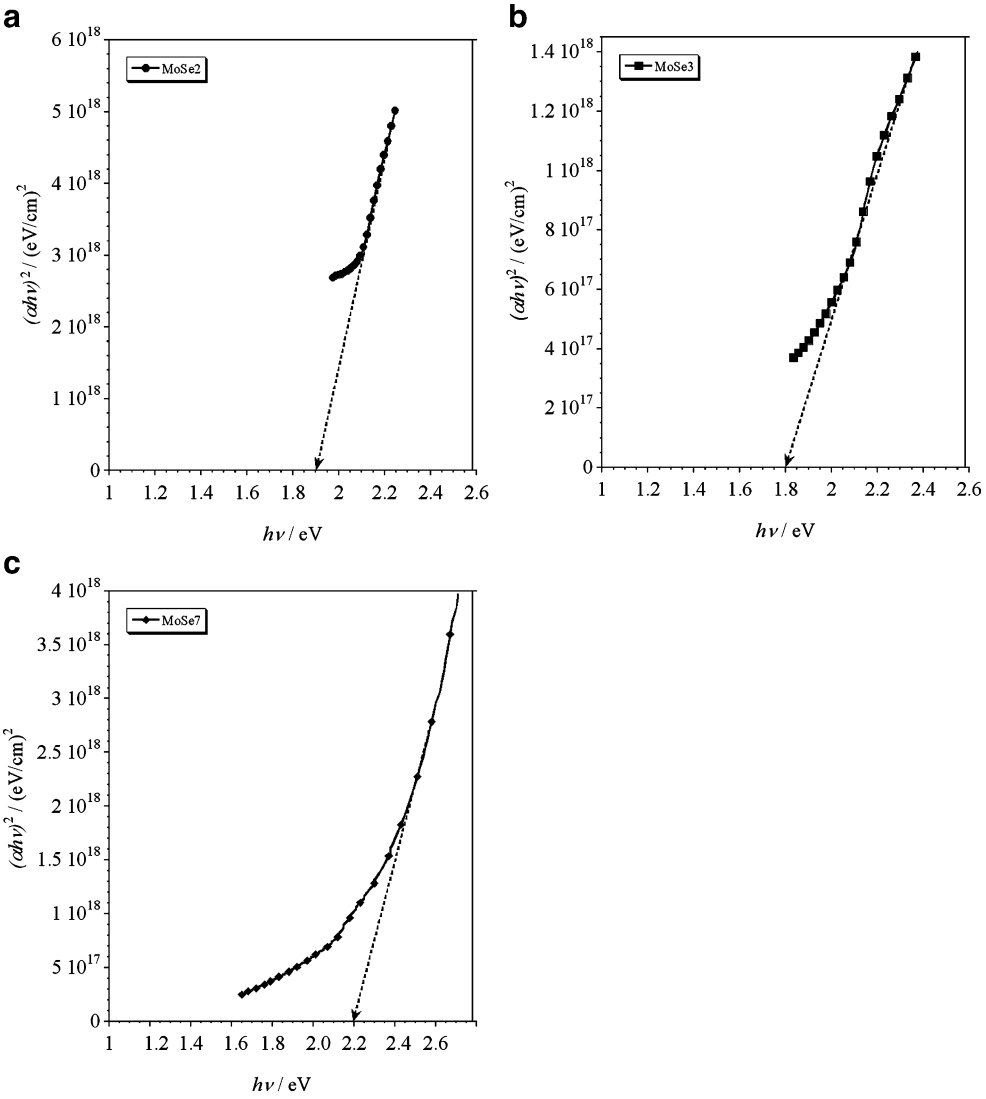

Fig. 12 $(\alpha h\nu)^2$ vs. $h\nu$ plots of MoSe2, MoSe3, and MoSe7 thin films. These correspond to **a** MoO_3, MoO_2, Se|MoO_3, MoO_2 (MoSe2); **b** MoO_3, MoO_2|MoO_2 (MoSe3); and **c** MoO_2 (MoSe7)

are 2 μm. Initial Se1 film is amorphous with no visible graininess, whereas molybdenum deposition results in particulate matter formation. Particle size seems to be decreasing with an increase in deposition potential as MoSe9 film deposited at −0.9 V has largest particle size of 86 nm, whereas MoSe4 and MoSe8 (−1.0 and −1.2 V, respectively), have average measured particle sizes of 50 and 40 nm, respectively. Root mean square roughness values of these films were very similar, 4.1, 4.4, 3.2, and 8.9 nm for Se1, MoSe4, and MoSe8, respectively, and 50 nm for MoSe9. These data show a transition between the amorphous selenium film and well-defined particle size molybdenum oxide films. There is no exact correlation, though, between deposition parameters and particle size.

Table 5 Optical characteristics of the deposited molybdenum oxide layers

	MoO_3, MoO_2, Se|MoO_3, MoO_2 (MoSe2)	MoO_3, MoO_2| MoO_2 (MoSe3)	MoO_2 (MoSe7)
Thickness, nm (WDM)[a]	130±5	205±3	272±6
Absorption edge, nm	600	650	560
α, $\times 10^{-4}$, cm^{-1}	8.18	3.46	4.65
E_{og}, eV	1.90	1.79	2.19

WDM weight difference method

[a] Three samples of each film were deposited, and thickness of each sample was calculated assuming MoO_2 density as the bulk density of deposited films.

UV–VIS studies

XPS depth profiling experiments indicated the formation of three different multilayer compositions of MoO_3, MoO_2, Se|MoO_3, MoO_2 (MoSe2), MoO_3, MoO_2|MoO_2 (MoSe3), and MoO_2 (MoSe7). The absorption spectra of these films were recorded in wavelength 350–1,100 nm at 293 K temperature (Fig. 11).

The absorption edge, depending on the film structure, was found to be within 560 and 650 nm. The optical absorption coefficient, α, was calculated from the absorbance, A, using the following equation [38]:

$$\alpha = 2.303\frac{A}{d} \tag{9}$$

where d is the sample thickness. Thickness was estimated using weight difference method. Three samples of each film were deposited, and thickness of each sample was calculated assuming the MoO_2 density as a bulk density of deposited film.

The absorption coefficient was of the order of 10^4 cm^{-1} above the absorption edge. Plots of $(\alpha h\nu)^2$ vs. $h\nu$ (Fig. 12) indicate direct allowed transitions are responsible for optical absorption. Extrapolation of the straight-line portion to the zero absorption (α=0) gave the values of the band gap energy (E_g). These are summarized in Table 5. The bandgap values obtained were between 1.79 and 2.19 eV, thus in the visible region. It can be proposed here that layered molybdenum oxide films can be deposited under controlled conditions with optical response properties in the visible region.

Conclusions

It has been demonstrated that molybdenum oxide films can be electrodeposited on Se|SnO_2|glass surface from alkaline citrate solutions containing 0.2 M Na_2MoO_2. The film growth and composition was time and potential dependant. Careful adjustment of deposition parameters allows depositing molybdenum oxide thin films with varying layered composition. XPS depth profiling experiments of samples indicates formation of several different layers within the thin films, such as: MoO_3, MoO_2, Se|MoO_3, MoO_2 (MoSe2), MoO_3, MoO_2|MoO_2 (MoSe3), and MoO_2 (MoSe7) with MoO_2 being major species. The absorption edge of thin-layered molybdenum oxides films was found to lie between 560 and 650 nm, and absorption coefficients were in the order of 10^4 cm^{-1} above the absorption edge. The value of the band gap was film composition dependent and varied between 1.79 and 2.19 eV.

Acknowledgments The authors gratefully acknowledge National Science Foundation grant CHE 0320387, the Central Microscopy Research Facility (CMRF) at the University of Iowa, and Kenneth Moore, Director of CMRF, for access to the XPS and SEM.

References

1. Yang P, Yan H, Mao S, Russo R, Johnson J, Saykally R, Morris N, Pham J, He R, Choi H-J (2002) Adv Funct Mater 12:323
2. Wu Y, Yan H, Huang M, Messer B, Song JH, Yang P (2002) Chem Eur J 8:1260
3. Hu J, Odom TW, Lieber CM (1999) Acc Chem Res 32:435
4. Chandra S, Sahu SN (1984) J Phys D Appl Phys 17:2115
5. Patil RS, Uplane MD, Patils PS (2006) Int J Electrochem Sci 3:259
6. Patil RS, Uplane MD, Patil PS (2006) Appl Surf Sci 252:8050
7. Bolivar H, Izquierdo S, Tremont R, Cabrera CR (2003) J Appl Electrochem 33:1191
8. Kosminsky L, Bertotti M (1999) J Electroanal Chem 471:37
9. Das D, Sen PK, Das K (2008) Electrochim Acta 54:289
10. Shembel E, Apostolova R, Nagirny V, Kirsanova I, Grebenkin P, Lytvyn P (2005) J Solid State Electrochem 9:96
11. Tian L, Liu L, Chen L, Lu N, Xu H (2005) Sens Actuators B B105:484
12. Ferroni M, Guidi V, Martinelli G, Nelli P, Sacerdoti M, Sberveglieri G (1997) Thin Solid Films 307:148
13. Pathak VM, Patel KD, Pathak RJ, Srivastava R (2002) Sol Energy Mater Sol Cells 73:117
14. Dye RC, Snow RC (2001) Thermally tolerant multilayer metal membrane Patent 6,214,090, USA
15. Rodriguez FJ, Sebastian PJ (1999) Int J Hydrogen Energy 25:243
16. Yufit V, Nathan M, Golodnitsky D, Peled E (2003) J Power Sources 122:169
17. Zach MP, Inazu K, Ng KH, Hemminger JC, Penner RM (2002) Chem Mater 14:3206
18. Pillai KC, Ilangovan G, Kumar SMS (2004) Proc Indian Natl Sci Acad A Phys Sci 70:503
19. McEvoy TM (2003) Electrochemical synthesis and nanoscale characterization of polymorphous molybdenum oxide. Thesis, Univ of Texas, Austin
20. McEvoy TM, Stevenson KJ (2004) J Mater Res 19:429
21. Banica R, Barvinschi P, Vaszilcsin N, Nyari T (2009) J Alloys Compd 483:402
22. Clayton CR, Lu YC (1989) Surf Interface Anal 14:66
23. Nakayama M, Komatsu H, Ozuka S, Ogura K (2005) Electrochim Acta 51:274
24. McEvoy TM, Stevenson KJ (2003) Anal Chim Acta 496:39
25. Nagirnyi VM, Apostolova RD, Shembel EM (2006) Russ J Appl Chem 79:1438
26. Baltrusaitis J, Usher CR, Grassian VH (2007) Phys Chem Chem Phys 9:3011
27. Fairley N (1999–2009) CasaXPS Version 2.3.14, www.casaxps.com
28. Rao GSR, Reddy SJ (1985) Acta Chim Hung 118:241
29. Pezzatini G, Loglio F, Innocenti M, Foresti ML (2003) Collect Czech Chem Commun 68:1579
30. Dukstiene N, Tatariskinaite L (2006) Pol J Chem 80:1715
31. Pourbaix MJN (1974) Atlas of Electrochemical Equilibriums in Aqueous Solutions 2nd ed. National Association of Corrosion Engineers Houston, TX
32. Badawy WA, Al-Kharafi FM (1998) Electrochim Acta 44:693
33. Takano I, Isobe S, Sasaki TA, Baba Y (1989) Appl Surf Sci 37:25
34. Swartz WE Jr, Hercules DM (1971) Anal Chem 43:1774
35. Yong YS, Howe RF, Hughes AE, Jaeger H, Sexton BA (1987) J Phys Chem 91:6331
36. Prabhakaran K, Sen P, Rao CNR (1986) Surf Sci 177:L971
37. Zhang X, He DH, Zhang QJ, Xu BQ, Zhu QM (2003) Chin Chem Lett 14:1066
38. Halimah MK, Daud WM, Sidek HAA, Zaidan AW, Zainal AS (2010) Mater Sci-Poland 28:173